Supporting Information for

Charge Gradients around Dendritic Voids Cause Nanoscale Inhomogeneities in Liquid Water

Tereza Schönfeldová[1], Nathan Dupertuis[1], Yixing Chen[1], Narjes Ansari[2], Emiliano Poli[3], David M. Wilkins[4], Ali Hassanali[3,#], Sylvie Roke[1,#]

[1]*Laboratory for fundamental BioPhotonics (LBP), Institute of Bio-engineering (IBI), and Institute of Materials Science (IMX), School of Engineering (STI), and Lausanne Centre for Ultrafast Science (LACUS), École Polytechnique Fédérale de Lausanne (EPFL), CH-1015, Lausanne, Switzerland,*

[2]*Italian Institute of Technology, Via Morego 30, 16163 Genova, Italy*

[3]*The Abdus Salam International Center For Theoretical Physics, Condensed Matter and Statistical Physics (CMSP)*

[4]*Atomistic Simulation Centre, School of Mathematics and Physics, Queen's University Belfast, Belfast BT7 1NN, Northern Ireland, United Kingdom*

[#]*ahassana@ictp.it; sylvie.roke@epfl.ch*,

Contents:

S1. Materials and Methods

Chemicals

Carbon tetrachloride (CCl_4, 99.9%, Sigma-Aldrich) was used as received without further purification. H_2O was purified by a Milli-Q UF-Plus instrument from Millipore, Inc., and it has an electrical resistivity of 18.2 MΩ·cm.

Femtosecond elastic second harmonic scattering (fs-SHS)

Figure 1A illustrates the fs-ESHS setup, already described in Ref. [1]. fs-ESHS measurements were performed using 190-fs laser pulses centered at 1028 nm with a 200kHz repetition rate. The polarization of input pulses was controlled by a Glan-Taylor polarizer (GT10-B, Thorlabs) in combination with a zero-order half-wave plate (WPH05M-1030). The filtered (FEL0750, Thorlabs) input pulses with a pulse energy of 0.3 μJ (incident laser power P = 60 mW) were focused into a cylindrical glass sample cell (inner diameter 4.2 mm) with a waist diameter of ~35 μm and a Rayleigh length of 0.94 mm. The scattered second harmonic light was collected with a plano-convex lens (f = 5 cm), and then filtered (ZET514/10x, Chroma), polarized (GT10-A, Thorlabs), and finally focused into a gated photomultiplier tube (H7421-40, Hamamatsu). The angle of acceptance for the signal collection was 3.4°. The scattering pattern was measured at a scanning step of 5°. Each data point was acquired with an acquisition time of 20 × 1 s and a gate width of 10 ns. In the specific case of backscattering measurements at 180°, a dichroic mirror (042-5130, Eksma) was placed with 45° angle in the path of the incoming beam, after the long-pass filter and just before the focusing lens in front of the sample cell. This allowed the incoming beam at 1028 nm to be transmitted and focused to the sample, while backscattered light at 514 nm was collimated again with the same lens and then reflected to the side of the setup by the dichroic mirror. This second harmonic light was then collected with the same combination of bandpass filter, Glan-Taylor polarizer, and PMT as for the forward scattering measurements. All measurements were performed in a temperature- and humidity- controlled room (T = 297 K; relative humidity, 26.0 %).

S2. Coherent and incoherent contribution to SHS

Second harmonic generation is a nonlinear optical process where two photons with the same frequency ω interact with a non-centrosymmetric medium to be converted into one photon of a doubled frequency 2ω. The measured SHS intensity can be generally described by the following sum [2]

$$I(2\omega) \propto N\left\{\left\langle\left(\beta_{ijk}^{(2)}\right)^2\right\rangle_{incoh} + \left\langle\left(\beta_{ijk}^{(2)}\right)^2\right\rangle_{coh}\right\} \quad \text{(S1)}$$

where N is the number density of molecules and $\beta_{ijk}^{(2)}$ is the tensor element of the second-order hyperpolarizability $\beta^{(2)}$. Here $\langle\rangle$ represents an ensemble orientational average over all involved molecules. The *incoh* and *coh* subscripts denote the incoherent and coherent contribution to SHS, respectively.

If we consider that all molecules in a liquid are individual scatterers, the SHS intensity can be expressed and decomposed into two terms as follows [3]:

$$I(2\omega) = \frac{cn\epsilon_0}{2}\left|\sum_{\nu}\vec{E}_{\nu}(2\omega)\right|^2 = \frac{cn\epsilon_0}{2}\left\{\sum_{\nu=\nu'}\left|\vec{E}_{\nu}(2\omega)\right|^2 + \sum_{\nu\neq\nu'}\vec{E}_{\nu}(2\omega)\vec{E}_{\nu'}^{*}(2\omega)e^{i\tilde{q}\left(\tilde{r}_{\nu}-\tilde{r}_{\nu'}\right)}\right\}, \text{(S2)}$$

where c is the speed of light in vacuum, ω is the frequency of the excitation light, $\tilde{q}$ is the momentum transfer in the SH emission process (also known as scattering vector) and $\tilde{r}$ is the position of a molecule. The subscript ν refers to a specific molecule.

The first term in Equations (S1, S2), also known as hyper-Rayleigh scattering (HRS), arises from the non-centrosymmetry of individual molecules, meaning that the electron distribution is anisotropic. In a molecular random distribution, individual contributions from the uncorrelated molecules are summed up incoherently as there is no fixed phase relationship between the SH fields they generate. The second part of the SH signal is coherent and originates at non-centrosymmetrically distributed molecules. The generated SH fields are summed up coherently with phase differences determined by the molecular correlations such as H-bonding or dipole-dipole interactions. Therefore, this term brings insight into the specific liquid structure. In a isotropic molecular distribution, the coherent contributions cancel each other out due to the symmetry, leaving only the incoherent terms. In order to obtain SH signal from orientationally-correlated molecules in liquids, femtosecond laser pulses have to be used, otherwise, the signal of those orientational correlations would disappear due to averaging over the duration of a longer laser pulse [4].

In the fs-ESHS experiments, the polarization combinations are described by three letters which refer to the collected SH beam (first letter) and the two excitation beams (second and third letter) while each beam can be polarized either perpendicular to the scattering plane (S) or parallel to it (P). Under the assumption of material isotropy, the HRS intensity in SSS and PPP polarization combinations is given by [3]:

$$I_{SSS}(2\omega) = \frac{cnk_0^4 N_m V E_y^4}{32\pi^2 \epsilon_0 R^2} \langle \left(\beta_{yyy}^{(2)}\right)^2 \rangle \tag{S3}$$

$$I_{PPP}(2\omega) = \frac{cnk_0^4 N_m V E_x^4}{32\pi^2 \epsilon_0 R^2} \left\{ \langle \left(\beta_{yyy}^{(2)}\right)^2 \rangle cos^2\theta_R + \langle \left(\beta_{yxx}^{(2)}\right)^2 \rangle sin^2\theta_R \right\} \tag{S4}$$

where c is the velocity of light in vacuum, n is the refractive index of air, k_0 is the second harmonic wave vector, N_m is the molecular density of the liquid, V is the volume of the liquid contributing to the SHS intensity, E_x and E_y are the incoming electric fields along the X and Y-direction of the laboratory frame, and R is the distance between the far-field observation position and the scattering position. θ_R is the scattering angle in the XZ plane, with respect to the Z direction.

S3. Exclusion of the possibility of an artifact

In order to exclude the polarization artifacts in our experiment, we recorded two-photon fluorescence scattering patterns of 40 μM trypan blue solution in the SSS and PPP polarization combinations. As the trypan blue molecules are uncorrelated at such a low concentration and fluorescence is an incoherent process, isotropic polarization-independent scattering patterns from this solution are expected. Figure S1A shows that both SSS and PPP patterns feature the same constant intensity over the scattering angle range and are identical with each other within the experimental errors, which confirms that our SHS setup is polarization-independent.

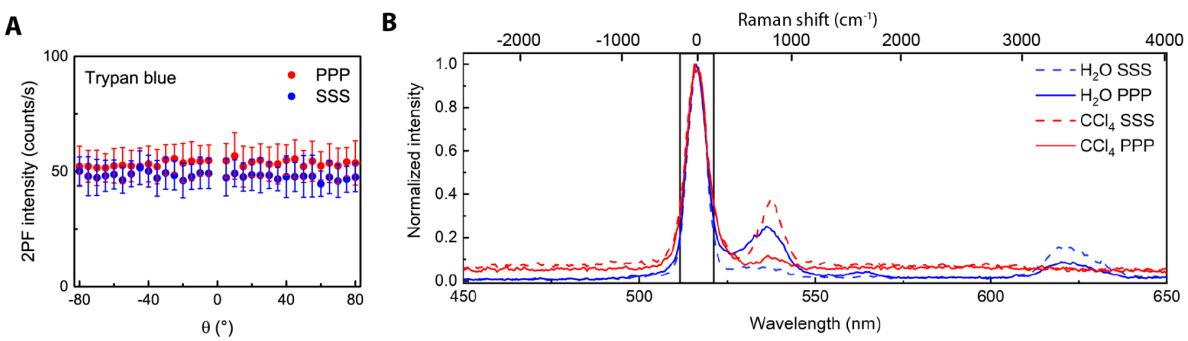

Figure S1: A: Two-photon fluorescence scattering patterns of 40 μM trypan blue in H_2O measured in the SSS (blue) and PPP (red) polarization combinations. The error bars represent the maximum standard deviation from 20 measurements. B: Spectra of H_2O and CCl4, respectively in the 5° direction with the fundamental wavelength at 1028 nm in SSS (dashed lines) and PPP (solid lines) polarization combination. The black rectangle indicates the 10 nm bandpass filter used for SH measurements.

To confirm that our measurements are not influenced by hyper-Raman signal, we measured spectra of CCl_4 and H_2O at a +5° scattering angle in PPP and SSS polarization combinations, see Figure S1B. It can be seen that all the hyper-Raman peaks are outside of the 10 nm bandpass filter (black rectangle) used for the SHS measurements.

Another concern that has to be taken into account is the measurement of elastic SH scattering as opposed to inelastic scattering. To be able to measure elastic scattering, fs laser pulses need to be used. Using nanosecond laser pulses leads to inelastic scattering and thus to laser-pulse induced water orientation, which will distort the experiment. This can be verified by comparing power dependencies of the SHS intensity for fs and ns laser pulses. For an elastic second-order process, the SH intensity / (power)^2 ratio should be constant. Figure S2 shows the measured power dependence for the scattered SH intensity comparing fs-ESHS experiments to ns-ESHS experiments [5]. It can be seen that fs experiments are elastic while the others are not. It means that any possible coherence observed in the ns and ps experiments cannot unambiguously be assigned to water-structural properties, as the laser pulses likely induce water-water correlations.

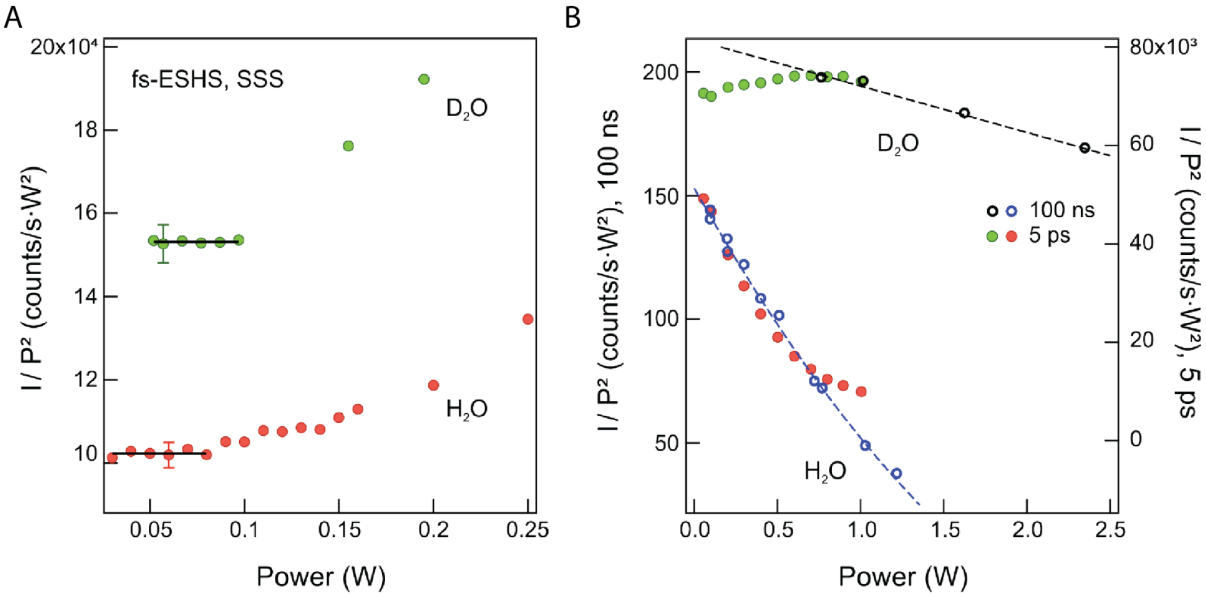

Figure S2. Plots of the measured intensity (I) divided by the square of the incident laser power as a function of the incident power (P). (**A**) The power dependence for an experiment employing 190 fs laser pulses in H_2O and D_2O (200 kHz, 35 μm beam waist). The solid black lines indicate the quadratic dependence of the SH intensity on the incident power. (**B**) The power dependence for experiments with 100 ns pulses (empty circles) from Ref.[6] and with 5 ps pulses (filled circles). The dashed lines indicate fitting with a quadratic function $a(1 + bP + cP^2)$ to the data from 100 ns measurements.

S4. Forward and backward scattering comparison

Figure 1A illustrates the SHS measurements from a top view. In this configuration, the momentum transfer ***q*** (also called the scattering vector) lies in the scattering plane and S polarization is always perpendicular to the scattering plane. Combining this knowledge with Equation (S2), we can see that the SSS polarization combination is only comprised of the incoherent contribution, whereas the PPP polarization combination contains not only the incoherent contribution, but also the coherent one, which shifts the PPP patterns above the SSS ones. To verify that the mismatch between the SSS and PPP patterns close to the forward direction is caused by the additional coherent response in the PPP polarization combination, we performed the SH measurements at the backward scattering direction, where the ***q*** vector is perpendicular to the P polarization.

The values of the PPP/SSS ratio when close to the forward direction (θ = 5°) and for the backward direction are displayed in Table S1. In the case of CCl_4, the PPP/SSS ratio is almost 1 for both directions, confirming the isotropy of this liquid at fs timescales. On the contrary, the PPP/SSS ratio for H_2O is significantly different for those two directions. This is a confirmation that the intermolecular correlations from hydrogen-bonding induce coherent signal, and the additional coherent signal contributes to PPP but not to SSS patterns.

Table S1: The ratios of the signal intensity in the PPP over the SSS polarization combination for H_2O and CCl_4, at near-forward (θ = 5°) and backward (θ = 180°) scattering direction.

PPP/SSS	H_2O	CCl_4
θ = 5°	1.35	0.95
θ = 180°	0.92	0.93

S5. MD simulations

Molecular dynamics simulations of TIP4P-EW [7] water (4096 molecules) were performed using the GROMACS 5.0 package [8] with a cubic box with an average side length of 49.68 Å. The system was equilibrated for 2 ns with a time step of 2 fs, and the final production run was carried out over another 40 ns using the NPT ensemble. The Nose-Hoover thermostat [9,10] and the Parrinello-Rahman barostat [11] were used to fix the system temperature and pressure at 300 K and 1 bar, with coupling time constants of 2 ps and 1 ps respectively. Ewald [12] summation was used to calculate the long-range electrostatic interactions, and a cutoff of 10 Å was used for the van-der- Waals interactions. In previous studies, we have also performed

extensive benchmarks across a range of different water models and shown that the presence of these large voids is consistently reproduced [13].

S6. Voronoi voids

The voids discussed in this work are the empty space within the hydrogen bond network of liquid water. To analyze the geometry of the empty space, we used the Voronoi-Delaunay method [14] which is implemented in the VNP code [15]. The interested reader is referred to Refs. [13,16] for more details. In summary, two radii named the probe (R_P) and bottleneck (R_B) radius are needed to construct the Voronoi voids. The former is used for identification of the empty space between the molecules and the latter for merging the connected regions. Here, we used R_P and R_B equal to 1.2 Å and 1.1 Å, respectively.

We have shown in previous studies that the presence of dendritic voids is a ubiquitous feature of a wide class of different water models. Figure S3 compares the maximal length of the void for four different empirical potentials of water namely MB-POL [17], TIP4P-EW [7], TIP4P-2005 [18] and SPC-E [19]. In all four cases we observe that

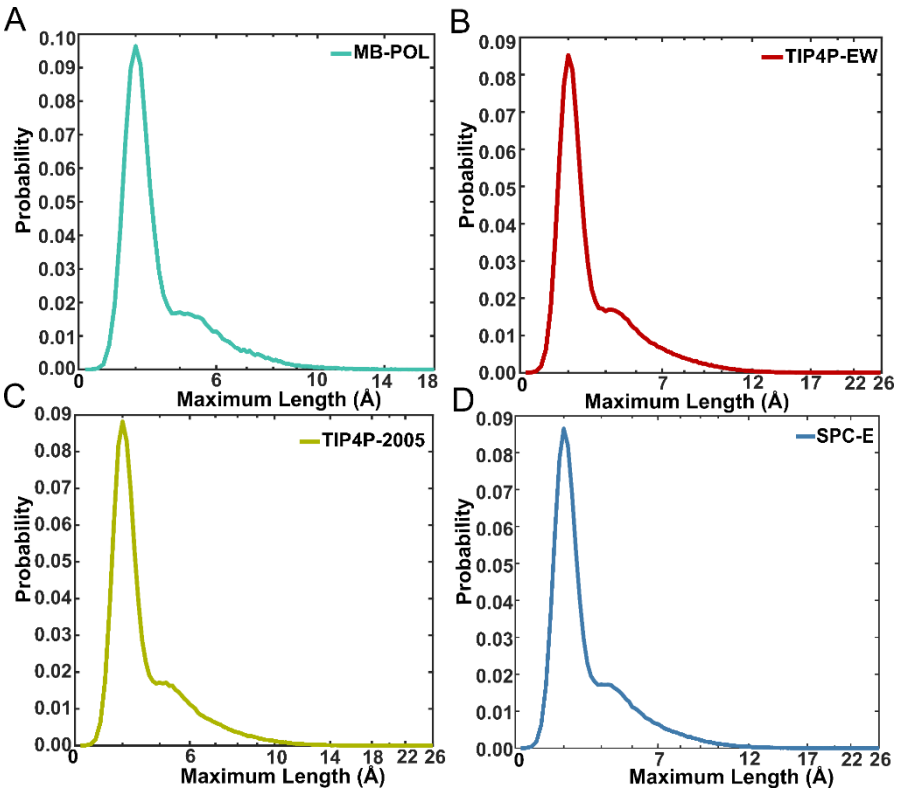

Figure S3. Plots of the distribution of the maximum length associated with a void for A) MB-pol, B) TIP4P-EW, C) TIP4P-2005 and D) SPC-E.

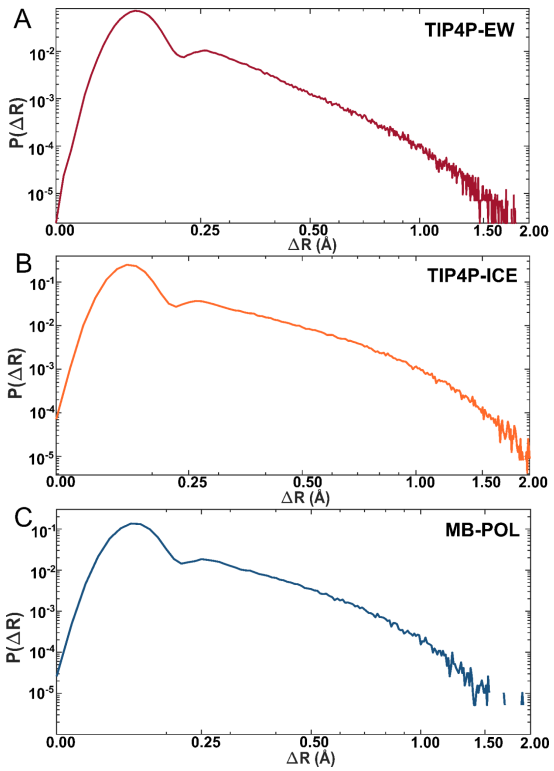

Figure S4. Plots of the distribution of the asphericity of a void for A) TIP4P-EW, B) TIP4P-ICE, and C) MB-POL.

there is a shoulder in the distribution which corresponds to the presence of non-spherical voids. There are of course subtle differences between the different models. For example, in MB-POL, one does not observe as large a tail in the maximum length due to the smaller size of the simulated box.

The distribution of the ΔR parameter, an asphericity parameter, is shown in Figure S4. We observe that in the three water models including MB-POL, very similar features are observed. Therefore, dendritic voids are generated by the following models: MP-POL, TIP4P-EW, SPC-E and TIP4P-ICE. MB-POL is currently considered the best computational model of non-dissociable water. Furthermore, the TIP4P-ICE water model was recently used to validate the existence of a second critical point in water [20]. These results prove that the existence of the dendritic voids is not an artefact of the water models.

S7. Linear scaling density functional theory (LS-DFT) calculations

In a recent work [21], we have shown that asymmetries in the hydrogen bond network around a water molecule can lead to an imbalance in charge transfer between hydrogen bonds being

accepted versus donated. Near the air-water interface where there is a breaking of symmetry in the hydrogen bond network, this leads to a triple layer of charge at the interface covering a length scale of 0.5 nm. In particular, we showed that topological defects in water which arise from fluctuations in the hydrogen bond network, serve as important sites for creating swings in the total charge of water molecules.

In this work, we show the coupling between the creation of transient voids (femtosecond) and charge gradients that form between water molecules around the voids. In order to do so, 20 frames were sampled from the TIP4P/EW simulations described earlier, and linear scaling density functional theory (LS-DFT) calculations were performed using the ONETEP code [22]. The LS-DFT calculations allow us to conduct electronic structure calculations of periodic boxes consisting of over 4000 water molecules. From the electron density, density derived electrostatic charges (DDEC) are used to assign net atomic charges to each atom and therefore determine the total charge of each water molecule. All technical details regarding the LS-DFT calculations and DDEC charges are documented in our previous work [13]. Here, we briefly summarize the main ideas.

LS-DFT as implemented in ONETEP, takes advantage of the near-sightedness of electrons in dealing with the density matrix representation of the system [23]. Essentially, the physical principle behind this is the fact that at constant chemical potential, properties such as the electron density $n(r)$ are strongly modulated by external potentials arising only from nearby points. By expanding the density matrix in terms of non-orthogonal generalized Wannier functions (NGWF) and applying a real-space cutoff, a sparse density matrix $\rho(r,r')$ is formed (see more details in [13]) allowing for the application of efficient diagonalization protocols.

In our LS-DFT simulations, the kinetic energy cutoff was 1000 eV and four NGWFs were used for O atoms and 1 NGWF was used for the H atoms. A localization radius of 10 Bohr was used in all cases. The DFT functional used for the simulations was the generalized gradient approximation (GGA) functional BLYP [24,25], along with Grimme's D2 correction functional [26]. The Kleinman–Bylander [27] norm-conserving pseudopotentials were used constructed using the Opium code [28].

DDEC charges are used to assign atomic charges derived from the underlying electron density. Specifically, the DDEC3 [29] scheme is used as implemented in the ONETEP code. The DDEC3 charges are built on ideas involving a combination of iterative Stockholder and iterative Hirshfield approaches. We have compared the DDEC charges we obtain to other charge schemes including Hirshfield and Natural Bond Order (NBO) charges and find that our results of the charge transfer being linked to the topology of the water molecules is consistently reproduced [13].

In our recent work [13], we performed extensive tests to determine how sensitive our results were to the use of standard GGA functionals (BLYP). Specifically, we compared the charge profiles obtained with BLYP to a hybrid functional B3LYP [24] as well as to a more accurate van-der-Waals functional rVV10 [30]. We also compared our results to wavefunction based approaches such as MP2 [31]. Finally, we also compared the charge profiles we got using configurations sampled from the most accurate potential for bulk water, MB-pol [32] and also various charge schemes (NBO and Iterative Hirshfield). Our results are consistently reproduced across all these various benchmarks.

S8. Hyperpolarizability Simulations

In order to estimate the SHS intensity arising from water molecules and voids, we focussed on the *incoherent* intensity of each subsystem, defined as,

$$I_{inc} = (1/N)|\beta_{XXZ}|^2, \qquad \text{(S5)}$$

where β_{XXZ} is the XXZ component of the hyperpolarizability tensor of the subsystem (i.e., molecule or void), with X the polarization vector of the incoming and Z the polarization vector of the outgoing light. *N* is the number of atoms in the subsystem. Eq. (S5) gives the contribution of the subsystem to the incoherent scattering intensity of a total system.

In order to remove the dependence of the intensity on the molecular orientation, it was averaged over all possible orientations of the subsystem to give the expression,

$$I_{inc} = (1/N) \sum_{ijk} \sum_{lmn} \beta_{ijk} \beta_{lmn} T_{ijklmn}, \qquad \text{(S6)}$$

where β_{ijk} is an element of the hyperpolarizability tensor in an axis system defined by the molecule or cluster, and ***T*** is a sparse 6-dimensional tensor whose elements depend on the incoming and outgoing polarization and can be determined by integrations over Euler angles as in Ref. [33].

We began by benchmarking the level of theory needed to correctly describe the hyperpolarizability intensity. We took 180 small clusters of 5 water molecules, comprising 60 in which a central molecule accepted and donated two hydrogen-bonds, 60 in which two H-bonds were donated and one accepted, and 60 in which one H-bond was donated and two were accepted. The hyperpolarizability for each cluster was computed using GAUSSIAN 2016 [34], at the MP2 and B3LYP levels of theory with a 6-311+G* basis set, and at the CCSD level (only for clusters donating one and accepting two hydrogen bonds). Fig. **S5** compares the results of the CCSD hyperpolarizability calculations with both the results of MP2 and of

B3LYP calculations. The agreement between CCSD and MP2 calculations of the hyperpolarizability is excellent, and while it is not as good between CCSD and B3LYP, there is an almost linear correlation between CCSD and B3LYP tensor elements. Even more important is the hyperpolarizability *intensity* arising from these individual responses, as these are to be compared with experiment.

The comparison between CCSD and MP2 for the small set of 60 clusters indicates that hyperpolarizabilities are already converged at the MP2 level. We then compared the hyperpolarizability intensity of Eq. (S6) for all 180 water clusters, using MP2 and B3LYP. Table **S2** shows this comparison, where it can be seen that not only does B3LYP preserve the ordering of intensities in the different types of water molecules, but the ratio between B3LYP and MP2 intensities is ~2.33 in all cases. Combining these results, we infer that B3LYP calculations can be used to make qualitative, and even semi-quantitative, statements about the SHS intensity of clusters containing water.

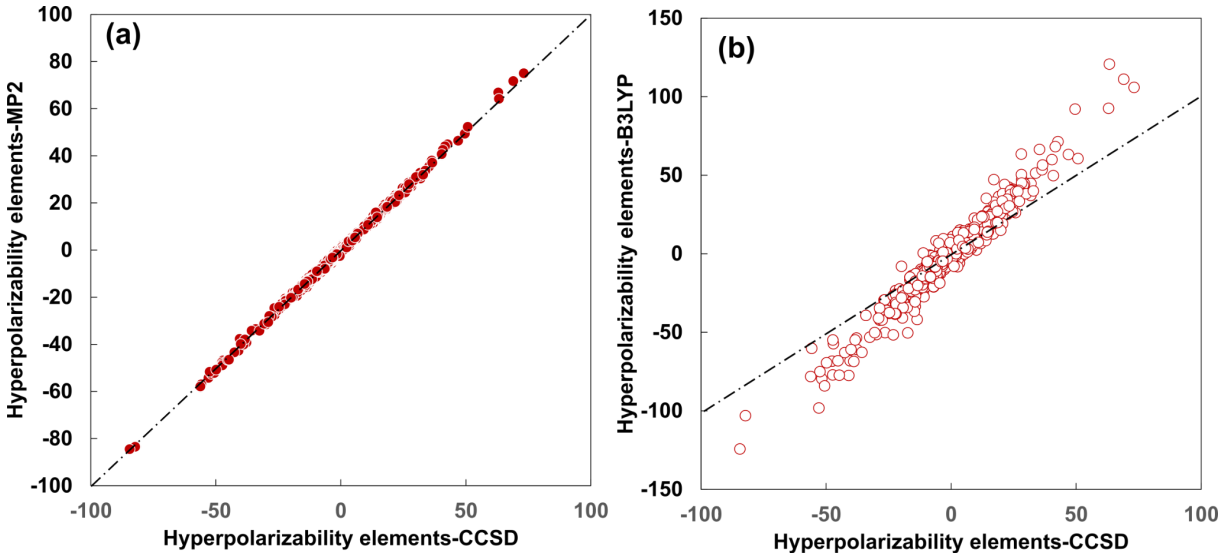

Figure S5. (a) Scatterplot of hyperpolarizability elements from CCSD calculations of clusters containing 5 water against the results of MP2 calculations. (b) Scatterplot of hyperpolarizability elements from CCSD calculations against the results of B3LYP calculations.

Table S2: Hyperpolarizability intensity of Eq. (S6) for water clusters. D12 indicates an average over 60 clusters donating one and accepting two H-bonds, D21 an average over 60 clusters donating two and accepting one H-bond, and D22 an average over 60 clusters donating two and accepting two H-bonds. These intensities are for a PPP scattering geometry.

Cluster type	B3LYP	MP2
D12	510.2	219.9

D21	601.9	258.6
D2	453.1	193.9

To obtain the results in Fig. 3A of the main text, the hyperpolarizability intensity was computed for a single water molecule at the B3LYP level, and for a set of 100 voids with 18 water molecules, 100 voids with 20 molecules, 100 voids with 25 molecules and 105 voids with 30 molecules. These voids were randomly selected from MD simulations.

References

(1) Gomopoulos, N.; Lütgebaucks, C.; Sun, Q.; Macias-Romero, C.; Roke, S. Label-Free Second Harmonic and Hyper Rayleigh Scattering with High Efficiency. *Opt. Express* **2013**, *21* (1), 815.

(2) Bersohn, R.; Pao, Y.; Frisch, H. L. Double-Quantum Light Scattering by Molecules. *J. Chem. Phys.* **1966**, *45* (9), 3184–3198.

(3) Chen, Y.; Roke, S. Generalized Expressions for Hyper-Rayleigh Scattering from Isotropic Liquids. ArXiv **2017,** arXiv:1705.04231.

(4) Fecko, C. J.; Eaves, J. D.; Loparo, J. J.; Tokmakoff, A.; Geissler, P. L. Ultrafast Hydrogen-Bond Dynamics in the Infrared Spectroscopy of Water. *Science* **2003**, *301* (5640), 1698–1702.

(5) Chen, Y.; Okur, H. I.; Dupertuis, N.; Dedic, J.; Wilkins, D. M.; Ceriotti, M.; Roke, S. Comment on "Water-Water Correlations in Electrolyte Solutions Probed by Hyper-Rayleigh Scattering" [J. Chem. Phys. 147, 214505 (2017)]. *J. Chem. Phys.* **2018**, *149*, 167101.

(6) Shelton, D. P. Water-Water Correlations in Electrolyte Solutions Probed by Hyper-Rayleigh Scattering. *J. Chem. Phys.* **2017**, *147* (21), 214505.

(7) Horn, H. W.; Swope, W. C.; Pitera, J. W.; Madura, J. D.; Dick, T. J.; Hura, G. L.; Head-Gordon, T. Development of an Improved Four-Site Water Model for Biomolecular Simulations: TIP4P-Ew. *J. Chem. Phys.* **2004**, *120* (20), 9665–9678.

(8) Abraham, M. J.; Murtola, T.; Schulz, R.; Páll, S.; Smith, J. C.; Hess, B.; Lindahl, E. GROMACS: High Performance Molecular Simulations through Multi-Level Parallelism from Laptops to Supercomputers. *SoftwareX* **2015**, *1–2*, 19–25.

(9) Nosé, S.; Klein, M. L. Constant Pressure Molecular Dynamics for Molecular Systems. *Mol. Phys.* **1983**, *50* (5), 1055–1076.

(10) Hoover, W. G. Canonical Dynamics: Equilibrium Phase-Space Distributions. *Phys. Rev. A* **1985**, *31* (3), 1695–1697.

(11) Parrinello, M.; Rahman, A. Polymorphic Transitions in Single Crystals: A New Molecular Dynamics Method. *J. Appl. Phys.* **1981**, *52* (12), 7182–7190.

(12) Darden, T.; York, D.; Pedersen, L. Particle Mesh Ewald: An N·log(N) Method for Ewald Sums in Large Systems. *J. Chem. Phys.* **1993**, *98* (12), 10089–10092.

(13) Ansari, N.; Dandekar, R.; Caravati, S.; Sosso, G. C.; Hassanali, A. High and Low Density Patches in Simulated Liquid Water. *J. Chem. Phys.* **2018**, *149* (20), 204507.

(14) Alinchenko, M. G.; Anikeenko, A. V.; Medvedev, N. N.; Voloshin, V. P.; Mezei, M.; Jedlovszky, P. Morphology of Voids in Molecular Systems. A Voronoi−Delaunay Analysis of a Simulated DMPC Membrane. *J. Phys. Chem. B* **2004**, *108* (49), 19056–19067.

(15) *The VNP Code*; 2016.

(16) Sosso, G. C.; Caravati, S.; Rotskoff, G.; Vaikuntanathan, S.; Hassanali, A. On the Role of Nonspherical Cavities in Short Length-Scale Density Fluctuations in Water. *J. Phys. Chem. A* **2017**, *121* (1), 370–380.

(17) Babin, V.; Leforestier, C.; Paesani, F. Development of a “First Principles” Water Potential with Flexible Monomers: Dimer Potential Energy Surface, VRT Spectrum, and Second Virial Coefficient. *J. Chem. Theory Comput.* **2013**, *9* (12), 5395–5403.
(18) Abascal, J. L. F.; Vega, C. A General Purpose Model for the Condensed Phases of Water: TIP4P/2005. *J Chem Phys* **2005**, *123*, 234505.
(19) Berendsen, H. J. C.; Grigera, J. R.; Straatsma, T. P. The Missing Term in Effective Pair Potentials. *J. Phys. Chem.* **1987**, *91* (24), 6269–6271.
(20) Debenedetti, P. G.; Sciortino, F.; Zerze, G. H. Second Critical Point in Two Realistic Models of Water. *Science* **2020**, *369* (6501), 289–292.
(21) Poli, E.; Jong, K. H.; Hassanali, A. Charge Transfer as a Ubiquitous Mechanism in Determining the Negative Charge at Hydrophobic Interfaces. *Nat. Commun.* **2020**, *11* (1).
(22) Skylaris, C.-K.; Haynes, P. D.; Mostofi, A. A.; Payne, M. C. Introducing ONETEP : Linear-Scaling Density Functional Simulations on Parallel Computers. *J. Chem. Phys.* **2005**, *122* (8), 084119.
(23) Prodan, E.; Kohn, W. Nearsightedness of Electronic Matter. *Proc. Natl. Sci.* **2005**, *102* (102), 11635–11638.
(24) Becke, A. D. Density-Functional Exchange-Energy Approximation with Correct Asymptotic Behavior. *Phys. Rev. A* **1988**, *38* (6), 3098–3100.
(25) Lee, C.; Yang, W.; Parr, R. G. Development of the Colle-Salvetti Correlation-Energy Formula into a Functional of the Electron Density. *Phys. Rev. B* **1988**, *37* (2), 785–789.
(26) Grimme, S. Semiempirical GGA-Type Density Functional Constructed with a Long-Range Dispersion Correction. *J. Comput. Chem.* **2006**, *27* (15), 1787–1799.
(27) Kleinman, L.; Bylander, D. M. Efficacious Form for Model Pseudopotentials. *Phys. Rev. Lett.* **1982**, *48* (20), 1425–1428.
(28) Rappe, A. M.; Rabe, K. M.; Kaxiras, E.; Joannopoulos, J. D. Optimized Pseudopotentials. *Phys. Rev. B* **1990**, *41* (2), 1227.
(29) Manz, T. A.; Sholl, D. S. Improved Atoms-in-Molecule Charge Partitioning Functional for Simultaneously Reproducing the Electrostatic Potential and Chemical States in Periodic and Nonperiodic Materials. *J. Chem. Theory Comput.* **2012**, *8* (8), 2844–2867.
(30) Vydrov, O. A.; Van Voorhis, T. Nonlocal van Der Waals Density Functional: The Simpler the Better. *J. Chem. Phys.* **2010**, *133* (24), 244103.
(31) Møller, C.; Plesset, M. S. Note on an Approximation Treatment for Many-Electron Systems. *Phys. Rev.* **1934**, *46* (7), 618.
(32) Cisneros, G. A.; Wikfeldt, K. T.; Ojamäe, L.; Lu, J.; Xu, Y.; Torabifard, H.; Bartók, A. P.; Csányi, G.; Molinero, V.; Paesani, F. Modeling Molecular Interactions in Water: From Pairwise to Many-Body Potential Energy Functions. *Chem. Rev.* **2016**, *116* (13), 7501–7528.
(33) Andrews, S. S. Using Rotational Averaging To Calculate the Bulk Response of Isotropic and Anisotropic Samples from Molecular Parameters. *J. Chem. Educ.* **2004**, *81* (6), 877.
(34) Frisch, M. J.; Trucks, G. W.; Schlegel, H. B.; Scuseria, G. E.; Robb, M. A.; Cheeseman, J. R.; Scalmani, G.; Barone, V.; Petersson, G. A.; Nakatsuji, H.; Li, X.; Caricato, M.; Marenich, A. V.; Bloino, J.; Janesko, B. G.; Gomperts, R.; Mennucci, B.; Hratchian, H. P.; Ortiz, J. V.; Izmaylov, A. F.; Sonnenberg, J. L.; Williams-Young, D.; Ding, F.; Lipparini, F.; Egidi, F.; Goings, J.; Peng, B.; Petrone, A.; Henderson, T.; Ranasinghe, D.; Zakrzewski, V. G.; Gao, J.; Rega, N.; Zheng, G.; Liang, W.; Hada, M.; Ehara, M.; Toyota, K.; Fukuda, R.; Hasegawa, J.; Ishida, M.; Nakajima, T.; Honda, Y.; Kitao, O.; Nakai, H.; Vreven, T.; Throssell, K.; Montgomery, J. A., Jr.; Peralta, J. E.; Ogliaro, F.; Bearpark, M. J.; Heyd, J. J.; Brothers, E. N.; Kudin, K. N.; Staroverov, V. N.; Keith, T. A.; Kobayashi, R.; Normand, J.; Raghavachari, K.; Rendell, A. P.; Burant, J. C.; Iyengar, S. S.; Tomasi, J.; Cossi, M.; Millam, J. M.; Klene, M.; Adamo, C.; Cammi, R.; Ochterski, J. W.; Martin, R. L.; Morokuma, K.; Farkas, O.; Foresman, J. B.; Fox, D. J. Gaussian 16 Revision C.01, 2016.